

Relativistic Impulse Approximation in Compton Scattering

Chen-Kai Qiao,¹ Hsin-Chang Chi,² Lei Zhang,¹ Peng Gu,¹ Cheng-Pang Liu,² Chang-Jian Tang,¹ Shin-Ted Lin,^{1,*} and Keh-Ning Huang^{3,4,†}

¹College of Physical Science and Technology, Sichuan University, Chengdu, Sichuan, 610065

²Department of Physics, National Dong Hwa University, Shoufeng, Hualien, 97401

³Institute of Atomic and Molecular Physics, Sichuan University, Chengdu, Sichuan, 610065

⁴Department of Physics, National Taiwan University, Taipei, 10617

(Dated: January 18, 2022)

We apply the relativistic impulse approximation to Compton scattering of atomic systems described using Dirac-Fock wavefunctions. An “exact” numerical treatment is employed in the integration, and calculations of C, Cu, Ge, and Xe atoms have been carried out. Comparisons with former treatments of relativistic impulse approximation are also provided on differential cross sections as well as Compton profiles, and notable discrepancies only arise away from the Compton peaks.

PACS numbers: 34.50.-s, 78.70.-g, 78.70.Ck, 31.15.xr, 32.90.+a, 95.35.+d

I. INTRODUCTION

Atomic Compton Scatterings have been widely investigated over the past few decades,

$$\hbar\omega_i + A \longrightarrow \hbar\omega_f + e^- + A^+ \quad (1)$$

through which many aspects of physics, *e.g.*, electron correlations, electron momentum distributions, X-ray as well as gamma-ray radiations, and Fermi surfaces, are revealed [1–11].

For convenience, Compton scattering is conventional approached using Klein-Nishina formula from the free electron approximation (FEA) [12, 13]. In FEA, electron interactions with atomic ions are neglected, and scattering electrons are also assumed to be rest prior to photon scatterings in the laboratory frame. In Klein-Nishina formula, the energy of the scattered photon ω_C is totally determined by its scattering angle θ via

$$\omega_C = \frac{\omega_i}{1 + \omega_i(1 - \cos\theta)/mc^2} \quad (2)$$

The Klein-Nishina formula works perfectly in the high-energy region, in which cases electrons are asymptotically free. However, in the low-energy region when the atomic effects come into play, the FEA becomes invalid and Klein-Nishina formula fails to explain the experiments.

Atomic effects are treated systematically in the impulse approximation (IA) [14–18], in which formulation, electrons in an atom have a momentum distribution. The motion of atomic electrons gives rise to a Doppler broadened Compton spectrum, as shown schematically in Fig I. In the former treatment of IA models, the doubly-differential cross section (DDCS) of Compton scatterings

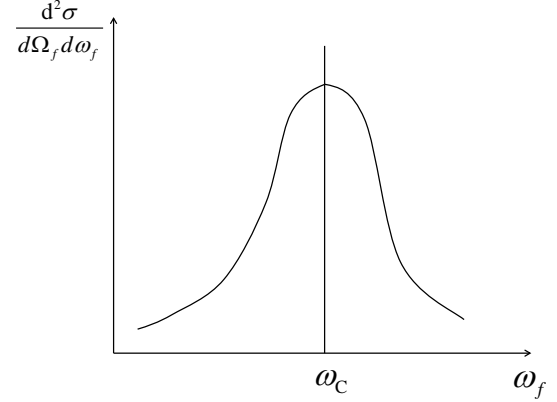


FIG. 1: Compton Spectrum in the IA model at a particular scattering angle θ .

can be factorized into two parts,

$$\left(\frac{d\sigma}{d\omega_f d\Omega_f} \right)_{IA} = Y \cdot J \quad (3)$$

where Y is a factor depend on kinematical and dynamical properties of Compton scatterings, irrelevant to the electronic structure of target materials. The correction factor J , called Compton profile, is related to the momentum distributions of electrons in the atomic or molecular ground state. This treatment has been widely applied to the studies of electron correlations in band structures, Fermi surfaces, and even has influences on low-energy threshold experiments in particle physics [3, 8, 19, 20]. The conclusions of these interdisciplinary researches depend strictly on the validity of factorization in Eq. (3).

Therefore, for a comprehensive study of atomic Compton Scattering processes, in this article we develop an “exact” numerical treatment of relativistic impulse approximation (RIA), without invoking the factorization in Eq. (3). Then we apply the present approach to Comp-

*Electronic address: stlin@scu.edu.cn

†Electronic address: knhuang1206@gmail.com

ton scattering with several atoms, and results are compared with former treatments of RIA. A carefully analysis on the adequacy of the former RIA treatments is provided in this work. In a recent paper, LaJohn have compared various treatments of RIA formulation in a similar way, and the nonrelativistic limit of RIA is achieved in the low-momentum-transfer cases [21]. However, LaJohn's work only limited to the hydrogen-like systems. In this work, more complicated atomic systems are taken into consideration. We apply the present scheme to atoms C, Cu, Ge, and Xe, which are chosen to represent elements in the small- Z , middle- Z , and large- Z regimes, respectively. Moreover, effective Compton profiles are proposed and analyzed to quantify the deviations between our results and those from former RIA treatments.

Recently, there are great interests in experimental detections of dark matter particles and neutrinoless double beta decays [23–34]. These experiments, which utilizing high-purity Germanium and Xenon detectors, need a sufficient low radiation background. Compton scattering is one of the most dominant radiation backgrounds for X-ray and gamma rays that must be suppressed and subtracted. Therefore studying the atomic Compton scattering effects in detectors shall have great impacts on these elementary particle experiments. Recent researches using former treatments of RIA have shown that low momentum transfer Compton scattering plays a significant role in dark matter direct detections [20]. Our method discussed here can be easily applied to this area and could have impacts and guidance on analyzing and subtraction of Compton scattering backgrounds in particle physics experiments.

This paper is organized as follows. Sec. II is devoted to introduce the RIA formulation and is divided into two subsections. In Sec. IIA, we briefly review the former treatments of Compton Scattering in the RIA formulation. In Sec. IIB, We describe our present numerical treatment of RIA for applications to atomic Compton scatterings. Results and comparisons of our approach with former RIA treatments are presented in Sec. III. Conclusions and future perspectives are given in Sec. IV.

II. RELATIVISTIC IMPULSE APPROXIMATION

A. Former Treatments

In this section, we give a description on former theoretical treatments of Compton Scatterings in the RIA formulation. The nonrelativistic impulse approximation approach can be derived similar to the relativistic case.

In the framework of RIA, consider an incident photon with energy ω_i and momentum \mathbf{k}_i scattering with an electron which has energy E_i and momentum \mathbf{p}_i . After scattering, the energy and momentum of emitted photon are ω_f and \mathbf{k}_f , and energy and momentum of final state electron are E_f and \mathbf{p}_f . Then the DDCS of Compton

scattering in RIA formulation is given by [15–17]

$$\frac{d^2\sigma}{d\omega_f d\Omega_f} = \frac{r_0^2 m^2 c^4}{2} \frac{\omega_f}{\omega_i} \iiint d^3p_i \rho(\mathbf{p}_i) \frac{X(K_i, K_f)}{E_i E_f} \delta(E_i + \omega_i - E_f - \omega_f) \quad (4)$$

where r_0 is the electron classical charge radius, functions K_i, K_f are defined as

$$K_i = k_i^\mu \cdot p_{i\mu} = \frac{E_i \cdot \omega_i}{c^2} - \mathbf{p}_i \cdot \mathbf{k}_i \quad (5)$$

$$\begin{aligned} K_f &= k_f^\mu \cdot p_{i\mu} = \frac{E_i \cdot \omega_f}{c^2} - \mathbf{p}_i \cdot \mathbf{k}_f \\ &= K_i - \frac{\omega_i \omega_f (1 - \cos \theta)}{c^2} \end{aligned} \quad (6)$$

and the kernel function $X(K_i, K_f)$ is defined as

$$\begin{aligned} X(K_i, K_f) &= \frac{K_i}{K_f} + \frac{K_f}{K_i} + 2m^2 c^2 \left(\frac{1}{K_i} - \frac{1}{K_f} \right) \\ &\quad + m^4 c^4 \left(\frac{1}{K_i} - \frac{1}{K_f} \right)^2 \end{aligned} \quad (7)$$

Here $\rho(\mathbf{p}_i)$ denotes the momentum distribution of electrons, which is related to the charge density $\rho(\mathbf{r})$ through Fourier transformation

$$\rho(\mathbf{p}_i) = \frac{1}{(2\pi)^{3/2}} \iiint d^3r \rho(\mathbf{r}) e^{i\mathbf{p}_i \cdot \mathbf{r}} \quad (8)$$

The electron's charge density is obtained by solving a manybody wavefunction of the atomic or molecular ground state

$$\rho(\mathbf{r}) = \sum_a |\psi_a(\mathbf{r})|^2 \quad (9)$$

where $\psi_a(\mathbf{r})$ is the individual wavefunction for a -th electron, and the sum is over all electrons.

In the previous works, Ribberfors *et al.* have found that the kernel function $X(K_i, K_f)$ in Eq. (4) is a slow-varying function and therefore can be pulled out of the integration [15, 17, 19]. Successively, this kernel is furthermore approximated by

$$\begin{aligned} X(K_i, K_f) &\approx \bar{X}(p_z) \\ &= \frac{K_i(p_z)}{K_f(p_z)} + \frac{K_f(p_z)}{K_i(p_z)} \\ &\quad + 2m^2 c^2 \left(\frac{1}{K_i(p_z)} - \frac{1}{K_f(p_z)} \right) \\ &\quad + m^4 c^4 \left(\frac{1}{K_i(p_z)} - \frac{1}{K_f(p_z)} \right)^2 \end{aligned} \quad (10)$$

where

$$K_i(p_z) = \frac{\omega_i E(p_z)}{c^2} + \frac{\omega_i (\omega_i - \omega_f \cos \theta) p_z}{c^2 q} \quad (11)$$

$$K_f(p_z) = K_i(p_z) - \frac{\omega_i \omega_f (1 - \cos \theta)}{c^2} \quad (12)$$

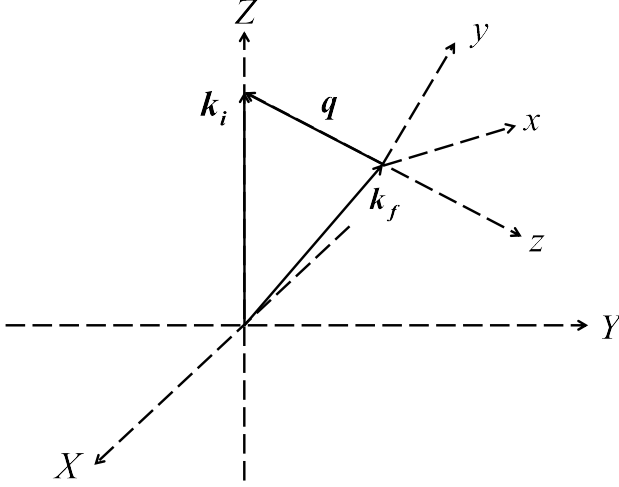


FIG. 2: Coordinate system XYZ and xyz . Coordinate system XYZ is chosen such that the Z axis is along the direction of initial photon \mathbf{k}_i , and X axis can be chosen as arbitrary direction perpendicular to the Z axis. The direction of scattered photon is denoted as \mathbf{k}_f , and the vectors \mathbf{q} is defined as $\mathbf{q} \equiv \mathbf{k}_i - \mathbf{k}_f$. The axis z represent the momentum transfer direction.

with $E(p_z) = \sqrt{m^2 c^4 + p_z^2 c^2}$ and q is the modulus of the momentum transfer vector $\mathbf{q} \equiv \mathbf{k}_i - \mathbf{k}_f$, and p_z is the projection of the electron's initial momentum on the momentum transfer direction

$$p_z = -\frac{\mathbf{p} \cdot \mathbf{q}}{q} = \frac{\omega_i \omega_f (1 - \cos \theta) - E(p_z)(\omega_i - \omega_f)}{c^2 q} \quad (13)$$

see Fig. 2 for more explanations. A good approximation to p_z can be made by

$$p_z \approx \frac{\omega_i \omega_f (1 - \cos \theta) - mc^2(\omega_i - \omega_f)}{c^2 q} \quad (14)$$

Moreover, p_z and $E(p_z)$ are related to the minimal energy and momentum values of the initial electron allowed in energy and momentum conservations

$$p_i^{\min} = |p_z|; \quad E_i^{\min} = E(p_z) \quad (15)$$

By these assumptions, the DDCCS of Compton scatterings in the former RIA treatments is given by

$$\left(\frac{d\sigma}{d\omega_f d\Omega_f} \right)_{RIA} = \frac{r_0^2}{2} \frac{m}{q} \frac{mc^2}{E(p_z)} \frac{\omega_f}{\omega_i} \bar{X}(p_z) J(p_z) = \bar{Y}^{RIA} \cdot J(p_z) \quad (16)$$

The same results can be derived from Eq. (4) through integration by part [15].

An alternative and more simpler approximation of kernel function $X(K_i, K_f)$ can be made by taking the $p_z \rightarrow 0$ limit of $\bar{X}(p_z)$, which is exactly its Klein-Nishina value [17, 18]

$$X(K_i, K_f) \approx X_{KN} = \frac{\omega_i}{\omega_f} + \frac{\omega_f}{\omega_i} - \sin^2 \theta \quad (17)$$

Therefore the simplified results of DDCCS for Compton scatterings in former RIA treatments can be expressed as

$$\left(\frac{d\sigma}{d\omega_f d\Omega_f} \right)_{RIA} = \frac{r_0^2}{2} \frac{m}{q} \frac{\omega_f}{\omega_i} X_{KN} J(p_z) = Y_{KN}^{RIA} \cdot J(p_z) \quad (18)$$

From Eqs. (16) and (18), it is obvious that the DDCCS of Compton scattering in former RIA treatments just factorize into two parts as in Eq. (3),

$$\left(\frac{d\sigma}{d\omega_f d\Omega_f} \right)_{RIA} = Y^{RIA} \cdot J(p_z) \quad (19)$$

The correction factor $J(p_z)$, which incorporate ground state electron momentum distribution, is Compton profile defined as

$$J(p_z) \equiv \iint \rho(\mathbf{p}) d p_x d p_y \quad (20)$$

For almost all the atoms, we assume that the momentum distribution is spherical symmetric, then atomic Compton profile simplifies to

$$J(p_z) = 2\pi \int_{|p_z|}^{\infty} p \rho(p) dp \quad (21)$$

In this case, the Compton profile $J(p_z)$ is bell-shaped and axisymmetric around the $p_z = 0$ axis. We will restrict ourselves to the spherical symmetric case in this paper.

B. “Exact” Numerical Treatments

In this section, we describe our “exact” numerical treatment for RIA formulation. Instead of treating the kernel function $X(K_i, K_f)$ to be a slow-varying function in the integration, we will evaluate directly the integral in Eq. (4) numerically.

The geometry of Compton scattering process efficient to numerical evaluation is displayed in Fig. 3. We choose a coordinate system XYZ such that the incoming photon moving towards the Z direction, the azimuthal angle and polar angle of outgoing photon, initial electron and final electron are denoted as (θ, ϕ) , (θ_1, ϕ_1) , (θ_2, ϕ_2) respectively. After employing such coordinate system, the function K_i and K_f can be calculated as

$$K_i = K_i(p_i, \theta_1) = \frac{E_i \omega_i}{c^2} - \frac{\omega_i p_i \cos \theta_1}{c} \quad (22)$$

$$K_f = K_f(p_i, \theta_1) = K_i(p_i, \theta_1) - \frac{\omega_i \omega_f (1 - \cos \theta)}{c^2} \quad (23)$$

From the energy and momentum conservations of the scattering process, the energy of scattered electron are

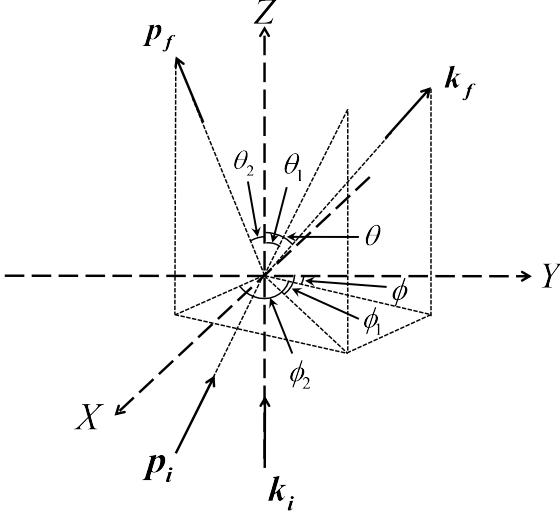


FIG. 3: Coordinate system XYZ used in the numerical evaluation. The Z axis is chosen to be the direction of initial photon \mathbf{k}_i as in Fig. 2. The direction of scattered photon is denoted as $\mathbf{k}_f = (k_f, \theta, \phi)$, and the vectors $\mathbf{p}_i = (p_i, \theta_1, \phi_1)$ and $\mathbf{p}_f = (p_f, \theta_2, \phi_2)$ represent the momentum of initial state and final state electron.

solved by

$$\begin{aligned}
 E_f &= E_f(p_i, \theta_1, \phi_1) \\
 &= \sqrt{p_i^2 c^2 + m^2 c^4 + \omega_i^2 + \omega_f^2 - 2\omega_i \omega_f \cos \theta} \\
 &\quad \frac{-2p_i c \omega_f [\cos \theta \cos \theta_1 + \sin \theta \sin \theta_1 \cos(\phi - \phi_1)]}{+2p_i c \omega_i \cos \theta_1}
 \end{aligned} \quad (24)$$

In this work, we focus ourselves to the simple atomic systems, molecular or condense matter systems are not taken into consideration. Moreover, Dirac-Fock ground state wavefunctions are employed to achieve electron's momentum distribution. Assuming that the atomic systems considered are spherical symmetric, the electron's momentum distribution then reduces to $\rho(\mathbf{p}_i) = \rho(p_i)$. In an actual calculation, the wavefunction of a particular electron is given by Dirac orbital $u_{njl}(r)$, which is composed of a large component G_{njl} and a small component F_{njl} . The Fourier transformation of large and small components give the momentum distributions:

$$\begin{aligned}
 \phi_{njl}^G(p) &= \sqrt{\frac{2}{\pi}} \int_0^\infty G_{njl}(r) j_l(pr) r^2 dr \\
 \phi_{njl}^F(p) &= \begin{cases} \sqrt{\frac{2}{\pi}} \int_0^\infty F_{njl}(r) j_{l+1}(pr) r^2 dr & j = l + \frac{1}{2} \\ \sqrt{\frac{2}{\pi}} \int_0^\infty F_{njl}(r) j_{l-1}(pr) r^2 dr & j = l - \frac{1}{2} \end{cases}
 \end{aligned} \quad (26)$$

and the total momentum distribution can be calculated

through

$$\begin{aligned}
 \rho(p_i) &= \sum_a |\phi_a(p)|^2 \\
 &= \sum_{njl} N_{njl} \left((\phi_{njl}^G(p_i))^2 + (\phi_{njl}^F(p_i))^2 \right)
 \end{aligned} \quad (27)$$

where N_{njl} is the number of electrons in each orbital (njl)

Putting Eqs (22), (23) and (27) into the integration in Eq. (4) and take atomic binding energies into account, we acquire the DDCCS for Compton scattering processes

$$\begin{aligned}
 \frac{d^2 \sigma}{d\omega_f d\Omega_f} &= \sum_{njl} \frac{d^2 \sigma_{njl}}{d\omega_f d\Omega_f} \\
 &= \sum_{njl} \frac{r_0^2}{2} \frac{\omega_f}{\omega_i} m^2 c^4 \Theta(\omega_i - E_{njl}^B) N_{njl} \\
 &\quad \iiint p_i^2 dp_i \sin \theta_1 d\theta_1 d\phi_1 \delta(E_i + \omega_i - E_f - \omega_f) \\
 &\quad \times \left((\phi_{njl}^G(p_i))^2 + (\phi_{njl}^F(p_i))^2 \right) \\
 &\quad \times \frac{X(K_i(p_i, \theta_1), K_f(p_i, \theta_1))}{E_i(p_i) E_f(p_i, \theta_1, \phi_1)}
 \end{aligned} \quad (28)$$

Where E_{njl}^B is the binding energy of orbital (njl), and $\Theta(\omega_i - E_{njl}^B)$ is the Heaviside step function. When the incident photon energy ω_i is less than atomic binding energy E_{njl}^B , the Heaviside step function prevents contributions from orbital (njl). In other words, electron in this orbital is inactive in atomic Compton scattering process $\hbar\omega_i + A \rightarrow \hbar\omega_f + e^- + A^+$.

In order to reach the final results of DDCCS numerically, one point should be mentioned. In Eq. (28), when integrating one of the there variables p_i , θ_1 and ϕ_1 , the Dirac delta function $\delta(E_i + \omega_i - E_f - \omega_f)$ in the integrand will restricts this variable to a fixed value. These fixed values \tilde{p}_i , $\tilde{\theta}_1$ and $\tilde{\phi}_1$ are solved by finding the zeros of function

$$f(p_i, \theta_1, \phi_1) = E_i(p_i) + \omega_i - E_f(p_i, \theta_1, \phi_1) - \omega_f \quad (29)$$

where $E_i(p_i) = \sqrt{p_i^2 c^2 + m^2 c^4}$ and $E_f(p_i, \theta_1, \phi_1)$ is calculated in Eq. (24)

To evaluate the integral in Eq. (28), we first integrate over the azimuthal angle ϕ_1 . After some redundant calculations routinely, we get the DDCCS for Compton scatterings:

$$\begin{aligned}
 \frac{d^2 \sigma}{d\omega_f d\Omega_f} &= \sum_{njl} \frac{r_0^2}{2\omega_i \sin \theta} m^2 c^4 \Theta(\omega_i - E_{njl}^B) N_{njl} \\
 &\quad \iint p_i dp_i d\theta_1 \left((\phi_{njl}^G(p_i))^2 + (\phi_{njl}^F(p_i))^2 \right) \\
 &\quad \times \frac{X(K_i(p_i, \theta_1), K_f(p_i, \theta_1))}{E_i(p_i) \times c \sqrt{1 - \cos^2(\phi - \tilde{\phi}_1)}}
 \end{aligned} \quad (30)$$

where the fixed azimuthal angle $\tilde{\phi}_1$ satisfies

$$\cos(\phi - \tilde{\phi}_1) = \frac{\omega_i^2 + \omega_f^2 - 2\omega_i\omega_f \cos \theta}{2p_i c \omega_f \sin \theta \sin \theta_1} - \frac{(\omega_i - \omega_f)^2}{2p_i c \omega_f \sin \theta \sin \theta_1} - \frac{(\omega_i - \omega_f)E_i(p_i)}{p_i c \omega_f \sin \theta \sin \theta_1} + \frac{\cos \theta_1 (\omega_i - \omega_f \cos \theta)}{\omega_f \sin \theta \sin \theta_1} \quad (31)$$

Moreover, only those which satisfied Eq. (31) and inequality $-1 \leq \tilde{\phi}_1 \leq 1$ simultaneously can be regarded as physical allowed value of $\tilde{\phi}_1$.

In this work, we adopt the above integration order in the numerical evaluation of Eq. (28). However, equivalent results can be achieved by integrating over momentum p_i or polar angle θ_1 first. Results from other integration orders are given in the Appendix A.

III. RESULTS AND DISCUSSIONS

In this section, we provide results on atomic Compton scattering using our “exact” numerical method of RIA described in Sec. II B. Detailed comparisons between our results and those from former treatments of RIA are presented. The validity of the factorization in Eq. (3) and available ranges of former RIA treatments are discussed through these comparisons. For a complementary study, we choose four neutral atoms C, Cu, Ge, and Xe to represent the small- Z , middle- Z , and large- Z regimes, respectively. Moreover, effective Compton profiles are extracted from our results to quantitatively illustrate the corrections of our method to the atomic Compton profile defined in Eq. (20).

A. Differential Cross Sections

In this subsection, we focus on the differential cross sections in atomic Compton scatterings. The DDSCS of Compton Scatterings with C, Cu, Ge, and Xe atoms at photon energy $\omega_i = 662$ KeV and scattering angle $\theta = 120^\circ$ are given as representative examples in Fig. 4. Comparative results between our “exact” numerical treatment and several former treatments of RIA have been displayed in this figure. The former RIA results are obtained through Eqs. (16) and (18), where the DDSCS of Compton scatterings factorized into factor Y times atomic Compton profiles J , while our results are acquired by directly evaluate the numerical integral in Eq. (4). The various curves in this figure represent: 1) solid lines represent our exact RIA results; 2) dashed lines represent the former RIA results employing Eq. (16) with exact p_z values calculated in Eq. (13); 3) dashed-dotted lines correspond to the former RIA results utilizing Eq. (16) with approximate p_z values computed in Eq. (14); 4) short-dashed lines correspond to the former RIA results using Eq. (18) with exact p_z values; 5) short-dotted

curves display the former RIA results calculated through Eq. (18) with approximate p_z values.

In this figure, it is obvious to know that our “exact” numerical treatment successfully reproduces the former RIA results near the Compton peak region $\omega_f \approx \omega_C$, for both C, Cu, Ge, and Xe elements. However, when the energy of scattered photon goes far away from the Compton peak region, discrepancies between our results and former RIA treatments become notable. Therefore, the available range for the former RIA treatments, which factorized the DDSCS into factor Y times atomic Compton profiles J through Eq. (3), is just near the Compton peak region. Moreover, when $\omega_f < \omega_C$, the several former RIA treatments overestimate the DDSCS of Compton scattering, while in the region $\omega_f > \omega_C$, our results acquire larger cross sections than the former RIA results. For several former RIA treatments, both the approximations of kernel function $X(K_i, K_f)$ and the values of p_z have great impacts on DDSCS of Compton scattering. Among these former treatments of RIA, only one utilized more accurate kernel function approximation $X(K_i, K_f) \approx \bar{X}(p_z)$ and employed exact p_z values, which correspond to dashed curves in Fig. 4, agrees well with our approach in the whole energy spectrum.

In order to check the validity of former RIA treatments through kernel function $X(K_i, K_f)$ directly, we explore the function $X(K_i, K_f)$ in Eq. (7) numerically, and the results are given in the Appendix B. Detailed analysis shows that the approximation $X(K_i, K_f) \approx X_{KN}$ in the derivation of former RIA treatments only works well in the Compton peak region $\omega_f \approx \omega_C$. When final photon energy goes far away from the Compton peak region, the approximation $X(K_i, K_f) \approx X_{KN}$ becomes inappropriate. This is consistent with our conclusions obtained from DDSCS of Compton scattering in Fig. 4, where former RIA results based on the approximation $X(K_i, K_f) \approx X_{KN}$ through Eq. (18) have notable discrepancies away from the Compton peak region, regardless of whether exact or approximate p_z values are employed. As an comparison, in the Appendix B, we will demonstrate that $X(K_i, K_f) \approx \bar{X}(p_z)$ is a more accurate kernel function approximation than $X(K_i, K_f) \approx X_{KN}$ when ω_f goes far away from the Compton peak region. This conclusion can also be revealed from DDSCS of Compton scattering displayed in Fig. 4, where former RIA results depending on $X(K_i, K_f) \approx \bar{X}(p_z)$ through Eq. (16) have less discrepancies than those employing $X(K_i, K_f) \approx X_{KN}$ through Eq. (18).

B. Effective Compton Profiles

In order to further compare the results between our method and former RIA treatments quantitatively, we

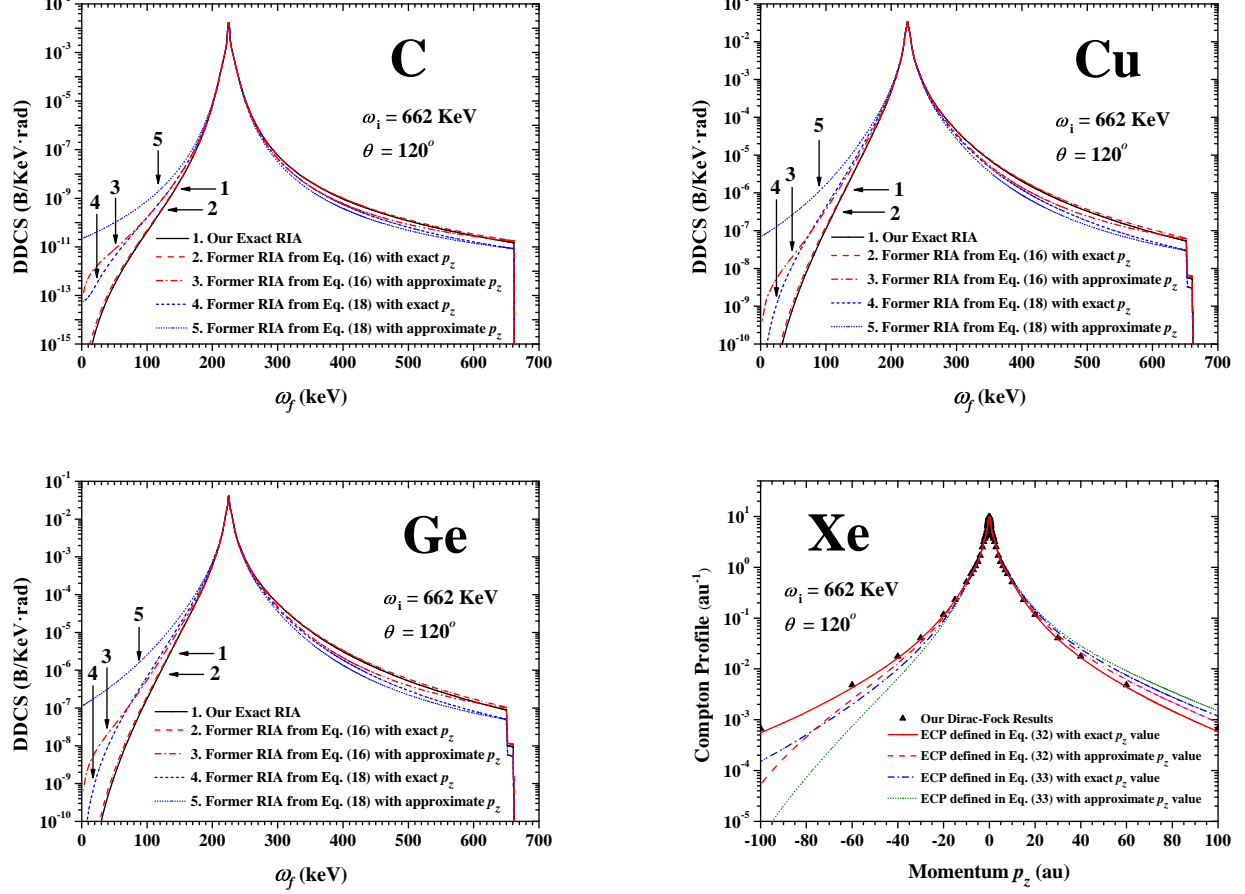


FIG. 4: DDSCS for Compton Scattering with C, Cu, Ge and Xe atoms at photon energy $\omega_i = 662$ KeV and scattering angle $\theta = 120^\circ$. Our results and results coming from several former treatments of RIA are displayed in the figure. The various curves in this figure represent: 1) solid lines represent our exact RIA results; 2) dashed lines represent the former RIA results employing Eq. (16) with exact p_z values calculated in Eq. (13); 3) dashed-dotted lines correspond to the former RIA results utilizing Eq. (16) with approximate p_z values computed in Eq. (14); 4) short-dashed lines correspond to the former RIA results using Eq. (18) with exact p_z values; 5) short-dotted curves display the former RIA results calculated through Eq. (18) with approximate p_z values.

can define the effective Compton profiles as

$$J_{\text{eff}}(p_z, \omega_i, \theta) \equiv \frac{1}{Y^{RIA}} \frac{d\sigma}{d\omega_f d\Omega_f} = \frac{2}{r_0^2} \frac{E(p_z)}{mc^2} \frac{q}{m} \frac{\omega_i}{\omega_f} \frac{\frac{d\sigma}{d\omega_f d\Omega_f}}{\bar{X}(p_z)} \quad (32)$$

and

$$J_{\text{sim-eff}}(p_z, \omega_i, \theta) \equiv \frac{1}{Y_{KN}^{RIA}} \frac{d\sigma}{d\omega_f d\Omega_f} = \frac{2}{r_0^2} \frac{q}{m} \frac{\omega_f}{\omega_i} \frac{\frac{d\sigma}{d\omega_f d\Omega_f}}{X_{KN}} \quad (33)$$

where p_z is projection of the electron's initial momentum on the momentum transfer direction defined in Eq. (13). The effective Compton profiles, when comparing with the

usual atomic Compton profiles in Eq. (20), give the corrections of our method to the former RIA treatments. It is worth noting that, the effective Compton profiles given in Eqs. (32) and (33) depend on three variables: projective momentum p_z , initial photon energy ω_i and scattering θ , while the atomic Compton profile defined in Eq. (20) is a single variable function of p_z .

Before going to any detailed analysis of effective Compton profiles, we should talk a little more about the variable p_z . As discussed in Sec. IIA, the projective momentum p_z can be calculated through its exact form in Eq. (13) or approximate form in Eq. (14). These situations, when combined with effective Compton profiles $J_{\text{eff}}(p_z, \omega_i, \theta)$ and $J_{\text{sim-eff}}(p_z, \omega_i, \theta)$ defined in Eqs. (32) and (33), give rise to the four kinds of effective Compton profiles.

The four kinds of effective Compton profiles for C, Cu, Ge, and Xe atoms at initial photon energy $\omega_i = 662$

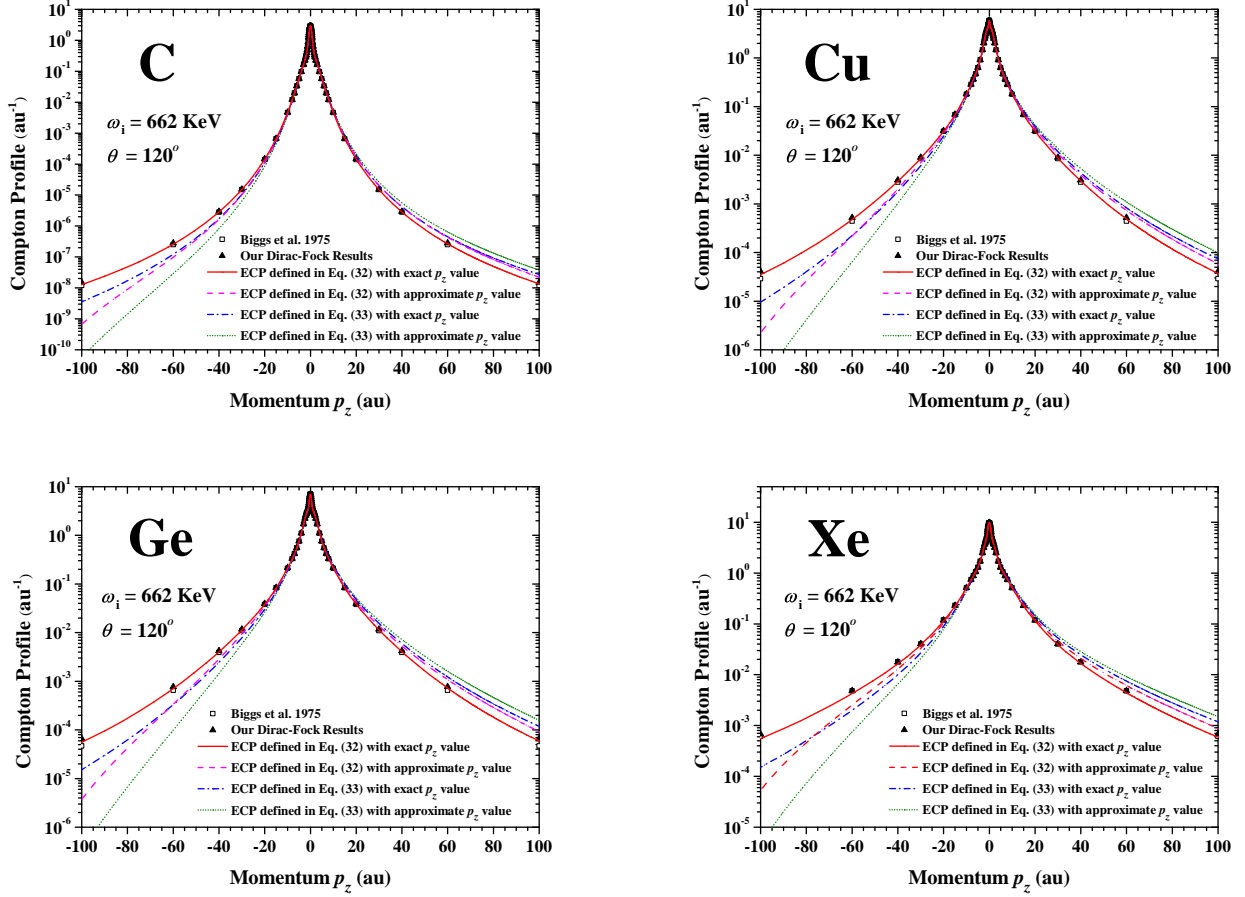


FIG. 5: Effective Compton profiles (ECP) for C, Cu, Ge and Xe atoms at photon energy $\omega_i = 662$ KeV with scattering angle $\theta = 120^\circ$. The solid lines correspond to the effective Compton profiles $J_{\text{eff}}(p_z, \omega_i, \theta)$ defined in Eq. (32) with exact p_z values calculated in Eq. (13). The dashed lines correspond to the effective Compton profiles $J_{\text{eff}}(p_z, \omega_i, \theta)$ defined in Eq. (32) with approximate p_z values computed in Eq. (14). The dashed-dotted lines represent the effective Compton profiles $J_{\text{sim-eff}}(p_z, \omega_i, \theta)$ defined in Eq. (33) with exact p_z values calculated in Eq. (13). The short-dotted lines represent the effective Compton profiles $J_{\text{sim-eff}}(p_z, \omega_i, \theta)$ defined in Eq. (33) with approximate p_z values computed in Eq. (14). Moreover, the atomic Compton profiles computed using Eq. (20) from nonrelativistic Hatree-Fock (HF) theory and relativistic Dirac-Fock (DF) theory are also presented. The HF results are given by Biggs *et al.* for $Z < 36$ [22], and DF results are computed using our program.

KeV and scattering angle $\theta = 120^\circ$ are plotted in Fig. 5. The solid lines correspond to the effective Compton profiles $J_{\text{eff}}(p_z, \omega_i, \theta)$ defined in Eq. (32) with exact p_z values calculated in Eq. (13). The dashed lines correspond to the effective Compton profiles $J_{\text{eff}}(p_z, \omega_i, \theta)$ defined in Eq. (32) with approximate p_z values computed in Eq. (14). The dashed-dotted lines represent the effective Compton profiles $J_{\text{sim-eff}}(p_z, \omega_i, \theta)$ defined in Eq. (33) with exact p_z values calculated in Eq. (13). The short-dotted lines represent the effective Compton profiles $J_{\text{sim-eff}}(p_z, \omega_i, \theta)$ defined in Eq. (33) with approximate p_z values computed in Eq. (14). The atomic Compton profiles computed using Eq. (20) from nonrelativistic Hatree-Fock theory and relativistic Dirac-Fock theory are also presented as comparisons. In the early years, Biggs *et al.* calculated the atomic Compton profile in the nonrelativistic Hatree-Fock theory for light el-

ements $Z < 36$ and in the relativistic Dirac-Fock theory for heavy elements $Z > 36$ [22]. In order to compare the nonrelativistic and relativistic results, we have recalculated the atomic Compton profiles for C, Cu, and Ge atoms in relativistic Dirac-Fock theory. We have found that, for small- Z element C with weak relativistic effects, there are no much differences between nonrelativistic and relativistic results; while for the middle- Z elements Cu and Ge, the relativistic effects become stronger and there are obvious differences between nonrelativistic and relativistic results for large value of $|p_z|$.

One observation from this picture that has significantly importance to interdisciplinary studies is that, when the projective momentum $|p_z|$ is less than 20 *a.u.*, all kinds of effective Compton profiles converge to the atomic Compton profiles. Therefore previous researches in condense matter physics, which studied electron momentum dis-

tributions or Fermi surfaces with the help of Compton profiles and Compton scattering experiments [1, 3–5, 8], still valid at a high level of accuracy, because researches in these areas mainly focus on the region $|p_z| \sim a.u.$. However, in the large $|p_z|$ regions, except for the effective Compton profiles $J_{\text{eff}}(p_z, \omega_i, \theta)$ defined in Eq. (32) employing exact p_z values, other effective Compton profiles all have large discrepancies with atomic Compton profiles at large momentum $|p_z|$, especially in the negative axis of p_z . This is consistent with our conclusions obtained from DDCS in Sec. III A, where large $|p_z|$ values correspond to cases where final photon energy ω_f move far away from the Compton peak region. In these situations, our results have notable differences with former RIA treatments. Another interesting phenomenon revealed in Fig. 5 is that, unlike the atomic Compton profiles, the effective Compton profiles generally are not axisymmetric around the $p_z = 0$ axis.

Furthermore, in this work, we have calculated all kinds of effective Compton profiles at different initial photon energy ω_i and scattering angle θ , and the results are presented in the Appendix C. In the Appendix C, we will see that the simplified version of effective Compton profiles $J_{\text{sim-eff}}(p_z, \omega_i, \theta)$ defined in Eq. (33) are more sensitive to the scattering angle θ than the incoming photon energy ω_i . And effective Compton profiles $J_{\text{sim-eff}}(p_z, \omega_i, \theta)$ acquired from smaller scattering angle θ are more approaching to the usual atomic Compton profiles, see Appendix C for more discussions.

IV. SUMMARY

Throughout this paper, we develop an “exact” numerical method to evaluate the integral in RIA formulation, without invoking other approximations used in the former treatments of RIA. Compton Scatterings for atomic systems are carefully analyzed in this work, and our results are compared with former treatments of RIA effectively. We have chosen four typical elements C, Cu, Ge and Xe to represent the small- Z , middle- Z and large- Z regimes respectively. For DDCS of Compton scatterings, our results agree with the former RIA treatments in the Compton peak region $\omega_f \approx \omega_C$. However, when the scattered photon ω_f moves far away from the Compton peak region, notable discrepancies are observed.

In order to further compare the corrections from our results to those from former RIA treatments quantitatively, several kinds of effective Compton profiles are defined in this work. Detailed results shown that except for the effective Compton profiles defined in Eq. (32) employed exact p_z values calculated in Eq. (13), other effective Compton profiles all have large discrepancies with atomic Compton profiles at large projective momentum $|p_z|$, especially in the negative axis of p_z . Moreover, by analyzing effective Compton profiles for various incident photon energies ω_i and scattering angles θ , we can draw the following conclusions:

(i). The effective Compton profiles does not shown any notable differences with atomic Compton profiles for small momentum value p_z , the discrepancies become significant only in the large momentum cases. Therefore researches in condense matter physics studying electron momentum distributions or Fermi surfaces with the help of Compton profiles and Compton scattering experiments, which correspond to $p_z \sim a.u.$, still valid with sufficient high precision.

(ii). Different from the atomic Compton profiles, the effective Compton profiles generally are not axisymmetric around the $p_z = 0$ axis.

(iii). The simplified version of effective Compton profiles $J_{\text{sim-eff}}(p_z, \omega_i, \theta)$ defined in Eq. (33) are more sensitive to the scattering angle θ than the incoming photon energy ω_i . Effective Compton profiles acquired from smaller scattering angle θ are more closer to the usual atomic Compton profiles.

In this work, we have carried out a complementary study of atomic Compton scatterings through our “exact” numerical treatment in the RIA formulation. However, in the past few years, several methods beyond IA framework have already been investigated [2, 6, 7, 35–40]. These researches, mainly employing low-energy theorems and S-matrix formulation, have revealed many remarkable and nontrivial aspects of Compton scatterings and have attracted lots of interests in interdisciplinary studies. We shall study atomic Compton Scatterings beyond IA formulation in the future.

ACKNOWLEDGMENTS

We acknowledge helpful discussions with Qiang Du and Henry T. Wong. This work was supported by the National Natural Science Foundation of China (Grants No. 11475117, No. 11474209), the National Key Basic Research Program (No. 2017YFA0402203) and the Fundamental Research Funds for the Central Universities.

Appendix A: Equivalent Results for Numerical Integration in Eq. (28)

In Sec. II B, we have mentioned that equivalent results for DDCS can be achieved by changing the integration order in Eq. (28). In this Appendix, we will give results on differential cross sections through other integration orders. When first integrating over momentum p_i or polar angle θ_1 in Eq. (28), the DDCS for Compton scattering

becomes

$$\begin{aligned} \frac{d^2\sigma}{d\omega_f d\Omega_f} &= \sum_{njl} \frac{r_0^2}{2} \frac{\omega_f}{\omega_i} m^2 c^4 \Theta(\omega_i - E_{njl}^B) N_{njl} \\ &\quad \iint \tilde{p}_i^2 \sin \theta_1 d\theta_1 d\phi_1 \left((\phi_{njl}^G(\tilde{p}_i))^2 + (\phi_{njl}^F(\tilde{p}_i))^2 \right) \\ &\quad \times \frac{X(K_i(\tilde{p}_i, \theta_1), K_f(\tilde{p}_i, \theta_1, \phi_1))}{E_i(\tilde{p}_i) E_f(\tilde{p}_i)} \\ &\quad \times \left| \frac{\tilde{p}_i c^2}{E_i(\tilde{p}_i)} - \frac{\tilde{p}_i c^2 + (A \sin \theta_1 - B \cos \theta_1) c}{E_f(\tilde{p}_i)} \right|^{-1} \end{aligned} \quad (A1)$$

$$\begin{aligned} \frac{d^2\sigma}{d\omega_f d\Omega_f} &= \sum_{njl} \frac{r_0^2}{2} \frac{\omega_f}{\omega_i} m^2 c^4 \Theta(\omega_i - E_{njl}^B) N_{njl} \\ &\quad \iint p_i dp_i d\phi_1 \left((\phi_{njl}^G(p_i))^2 + (\phi_{njl}^F(p_i))^2 \right) \\ &\quad \times \left| \frac{X(K_i(p_i, \tilde{\theta}_1), K_f(p_i, \tilde{\theta}_1, \phi_1)) \times \sin \tilde{\theta}_1}{E_i(p_i) \times (A \sin \tilde{\theta}_1 + B \cos \tilde{\theta}_1) c} \right| \end{aligned} \quad (A2)$$

where

$$A \equiv \omega_i - \omega_f \cos \theta \quad (A3)$$

$$B \equiv \omega_f \sin \theta \cos(\phi - \phi_1) \quad (A4)$$

The fixed momentum \tilde{p}_i and polar angle $\tilde{\theta}_1$ are calculated by solving the zeros of function f in Eq. (29) respectively. After routine calculations, \tilde{p}_i can be expressed as:

$$\tilde{p}_i = \frac{-MN \pm \sqrt{N^2 + (M^2 - 1)m^2 c^4}}{c(M^2 - 1)} \quad (A5)$$

where

$$M \equiv \frac{A \cos \theta_1 - B \sin \theta_1}{\omega_i - \omega_f} \quad (A6)$$

$$N \equiv \frac{\omega_i \omega_f (1 - \cos \theta)}{\omega_i - \omega_f} \quad (A7)$$

Similar to the cases of $\tilde{\phi}_1$ discussed in Sec. II B, only \tilde{p}_i which satisfied Eq. (A5) and $\tilde{p}_i \geq 0$ simultaneously can be regarded as physical allowed values.

The fixed polar angle $\tilde{\theta}_1$ can be expressed through $\sin \tilde{\theta}_1$ or $\cos \tilde{\theta}_1$. The expression for $\sin \tilde{\theta}_1$ and $\cos \tilde{\theta}_1$ are:

$$\sin \tilde{\theta}_1 = \frac{-BC \pm \sqrt{A^2(A^2 + B^2 - C^2)}}{A^2 + B^2} \quad (A8)$$

$$\cos \tilde{\theta}_1 = \frac{B}{A} \sin \tilde{\theta}_1 + \frac{C}{A} \quad (A9)$$

where C is defined as

$$C \equiv \frac{E_i(p_i)(\omega_i - \omega_f) - \omega_i \omega_f (1 - \cos \theta)}{p_i c} \quad (A10)$$

Furthermore, only for $\tilde{\theta}_1$ satisfied the above expressions and inequality $-1 \leq \tilde{p}_i \leq 1$ simultaneously are physically reasonable.

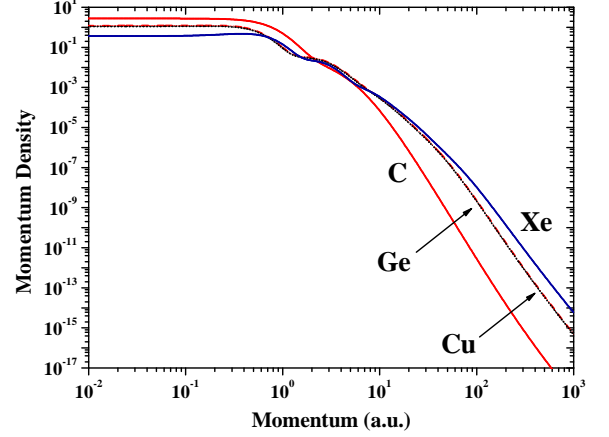


FIG. 6: Logarithmic diagram of electron momentum distributions $\rho(p_i)/Z$ for C, Ge, Cu and Xe atoms in the atomic units. It is worthy noting that we have normalized the momentum distribution into the contribution from per electron.

Appendix B: Validity of Approximation

$X(K_i, K_f) \approx X_{KN}$ and $X(K_i, K_f) \approx \bar{X}(p_z)$

In this Appendix, we will discuss the kernel function $X(K_i, K_f)$ in the integrand of Eq. (4), testing the validity of the approximations

$$X(K_i, K_f) \approx X_{KN} = \frac{\omega_i}{\omega_f} + \frac{\omega_f}{\omega_i} - \sin^2 \theta \quad (B1)$$

and

$$\begin{aligned} X(K_i, K_f) &\approx \bar{X}(p_z) \\ &= \frac{K_i(p_z)}{K_f(p_z)} + \frac{K_f(p_z)}{K_i(p_z)} \\ &\quad + 2m^2 c^2 \left(\frac{1}{K_i(p_z)} - \frac{1}{K_f(p_z)} \right) \\ &\quad + m^4 c^4 \left(\frac{1}{K_i(p_z)} - \frac{1}{K_f(p_z)} \right)^2 \end{aligned} \quad (B2)$$

in the former treatments of RIA discussed in Sec. II. In order to quantitatively describe the discrepancies between kernel function $X(K_i, K_f)$ and its Klein-Nishina value X_{KN} as well as its “averaged” value $\bar{X}(p_z)$, we define the relative factors α and β to be

$$\alpha \equiv \frac{X(K_i, K_f)}{X_{KN}} \quad (B3)$$

$$\beta \equiv \frac{X(K_i, K_f)}{\bar{X}(p_z)} \quad (B4)$$

The function $X(K_i, K_f)$ is calculated in Eq. (7), in general it depends on the initial and final photon energy ω_i and ω_f , scattering angle θ , as well as the electron pre-collision momentum $\mathbf{p}_i = (p_i, \theta_1, \phi_1)$. While the “averaged” value $\bar{X}(p_z)$ depends on projective momentum p_z

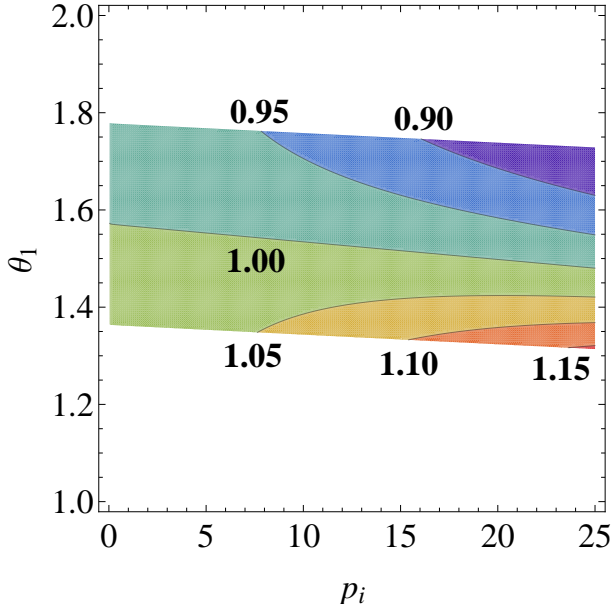


FIG. 7: Counterplot of relative factor α when final photon energy ω_f goes in the Compton peak region. When have chosen the energies to be $\omega_i = 662$ KeV, $\omega_f = \omega_C = 224.9$ KeV and scattering angle $\theta = 120^\circ$. The horizontal axis labels the electron momentum p_i in units of *a.u.*, and the vertical axis labels the polar angle of electron θ_1 in units of *rad*. The regions which are not kinematically allowed in the energy and momentum conservations are left with white.

obtained in Eqs. (13) or (14), irrespective of the transverse momentum in the *xy* plane, as well as polar and azimuthal angles. The Klein-Nishina value X_{KN} correspond to the special case where the electrons are at rest in the target $p_i = 0$.

Before going to any detailed analysis, we first give electron momentum distributions $\rho(p_i)/Z$ for C, Cu, Ge and Xe atoms in Fig. 6. In this figure, momentum distribution of each element has been normalized into the contribution from per electron. The momentum distributions of Cu and Ge atoms are very similar that can hardly be distinguished in the logarithmic coordinate. For all the four elements C, Cu, Ge and Xe, momentum distributions decrease rapidly in large momentum region. Therefore large momentum values give negligible contributions in the momentum distributions, compared with small momentum values. This indicate that small momentum region plays a dominant roles in the DDCS of Compton scatterings in Eq. (28), while large momentum have tiny contributions in the integration. Contributions from large momentum regions become notable only when the small momentum values are forbidden in the energy and momentum conservations.

We will choose the case $\omega_i = 662$ KeV and $\theta = 120^\circ$ as an representative example, analyzing the numerical results of α and β when final photon energy ω_f moves in and away from the Compton peak region respectively. First, we consider the case correspond to the Com-

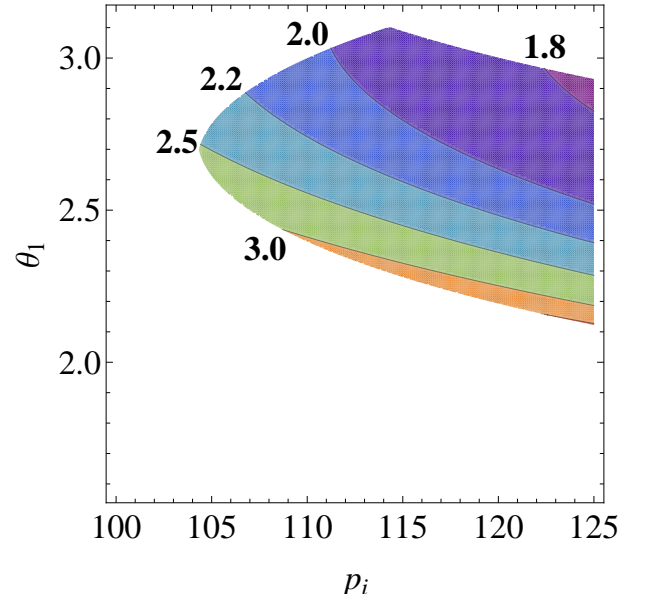


FIG. 8: Counterplot of relative factor α when final photon energy ω_f goes far away from the Compton peak region. We have chosen the energies to be $\omega_i = 662$ KeV, $\omega_f = 500$ KeV and scattering angle $\theta = 120^\circ$. The horizontal and vertical axes label electron momentum p_i and polar angle θ_1 as in Fig. 7. The regions which are not kinematically allowed in the energy and momentum conservations are left with white as in Fig. 7.

ton peak region, where final photon energy is chosen as $\omega_f = \omega_C = 224.9$ KeV. In this case, the projective momentum gives $p_z = 0$, which leads to $\bar{X}(p_z) = X_{KN}$, therefore relative factors α and β coincide with each other and only one of them need to be analyzed quantitatively. The numerical values of factor α in the Compton peak region are shown in Fig. 7. In this case, the minimal momentum value that is kinematically allowed becomes $p_i^{\min} = |p_z| = 0$ *a.u.*, which is given in Eq. (15). Therefore in this figure we only plot the contributions from small momentum values $p_i = 0 - 25$ *a.u.*, where the momentum density is sufficient large and can give notable contributions in the integration of Eq. (4). From the figure, we can observe that the relative factor α varies from 0.90 – 1.10 in this case, which demonstrate the validity of approximation $X(K_i, K_f) \approx X_{KN}$ and $X(K_i, K_f) \approx \bar{X}(p_z)$ in the Compton peak region. This is consistent with our DDCS results in Fig. 4, where our method successfully reproduces the former RIA results in the Compton peak region $\omega_f \approx \omega_C$.

On the other hand, we choose $\omega_f = 500$ KeV as an example to illustrate the cases when final photon energy goes far away from the Compton peak region. The results of relative factors α and β are give in Figs. 8 and 9. A crucial fact different from the previous case is that small momentum values $p_i < 100$ *a.u.* are not kinematically allowed in the energy and momentum conservations, therefore we only plot the regions where electron

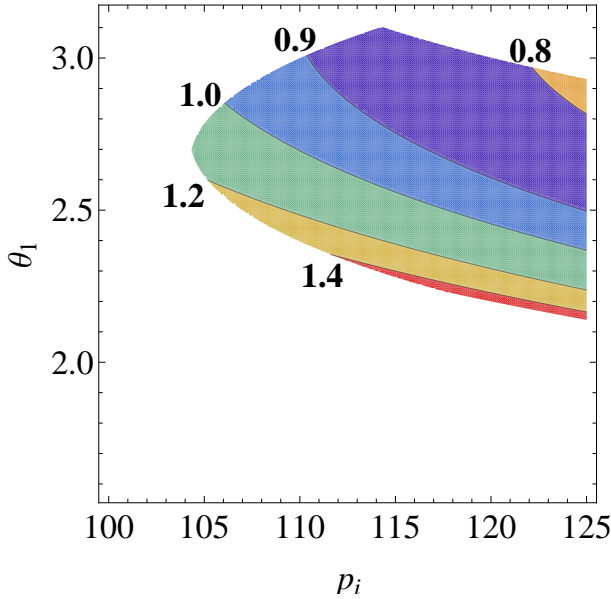


FIG. 9: Counterplot of relative factor β when final photon energy ω_f goes far away from the Compton peak region. We have chosen the energies to be $\omega_i = 662$ KeV, $\omega_f = 500$ KeV and scattering angle $\theta = 120^\circ$. The horizontal and vertical axes label electron momentum p_i and polar angle θ_1 as in Fig. 7. The regions which are not kinematically allowed in the energy and momentum conservations are left with white as in Fig. 7.

momentum density has sufficient large values. The minimal momentum value calculated through Eq. (15) is $p_i^{\min} = |p_z| \approx 105$ a.u.. From the figures, we can observe that the relative factor α varies from 1.8 – 3.5 in this region, while β is between 0.8 – 1.4, indicating that $X(K_i, K_f) \approx \bar{X}(p_z)$ is a better kernel function approximation than $X(K_i, K_f) \approx X_{KN}$. This is consistent with our DDCS results from Fig. 4 in Sec. III A, when the final photon energy moves away from the Compton peak region, the former RIA treatments agree with our results only when $X(K_i, K_f) \approx \bar{X}(p_z)$ is adopted in calculating the DDCS in Eq. (16) with exact p_z values utilized. When $X(K_i, K_f) \approx X_{KN}$ is adopted in the DDCS in Eq. (18), there are large discrepancies between our results and former RIA results, regardless of whether exact or approximate p_z values are employed.

Appendix C: More Results on Effective Compton Profiles

In this Appendix, we will display more detailed numerical results on the effective Compton profiles $J_{\text{eff}}(p_z, \omega_i, \theta)$ and $J_{\text{sim-eff}}(p_z, \omega_i, \theta)$ defined in Sec. III B. These results will reveal some intrinsic properties of various kinds of effective Compton profiles. For simplicity, we only list results for Ge atom. The cases for C, Cu, and Xe atoms are similar with those of Ge atom.

The effective Compton profiles for Ge atom at scat-

tering angle $\theta = 120^\circ$ with various incident photon energy are given in Fig. 10. In this work, we pick several characteristic energies from gamma ray sources: 320, 356, 511, and 662 KeV. The effective Compton profiles $J_{\text{eff}}(p_z, \omega_i, \theta)$ defined in Eq. (32) with approximate or exact p_z values computed in Eq. (14) and Eq. (13) are shown in the upper panels. While the lower panels plotted the effective Compton profiles $J_{\text{sim-eff}}(p_z, \omega_i, \theta)$ defined in Eq. (33) with approximate or exact p_z values. The atomic Compton profiles computed using Eq. (20) from nonrelativistic Hatree-Fock theory and relativistic Dirac-Fock theory are also presented as comparisons. From the figure, we can observe that, except that effective Compton profiles $J_{\text{eff}}(p_z, \omega_i, \theta)$ defined in Eq. (32) with exact p_z values fit well with atomic Compton profiles at all p_z values, other kinds of effective Compton profiles are not axisymmetric around the $p_z = 0$ axis and have large discrepancies at large $|p_z|$ values, especially in the negative axis of p_z . It worth noting that, for various kinds of effective Compton profiles, the projective momentum p_z has maximum and minimum values due to the energy and momentum conservations in Compton scatterings. Moreover, for the fixed angle θ , when the incident photon energy ω_i is lower, the maximal kinematically allowed value of p_z becomes smaller. In all situations, the minimum values of p_z are all less than -100 a.u., which is not shown in this figure. The same as in Sec. III B, when $|p_z|$ is small, various kinds of effective Compton profiles all fit well with the nonrelativistic and relativistic atomic Compton profiles. Large deviations only arise when $|p_z|$ is over 20 a.u., that correspond to the cases where final photon energy ω_f goes far away from the Compton peak region in the DDCS spectrum. Therefore previous researches in condense matter physics, which studied electron momentum distributions or Fermi surfaces with the help of Compton profiles and Compton scattering experiments, still reliable at a high level of accuracy [1, 3–5, 8]. Another interesting phenomenon is that all kinds of effective Compton profiles at different energies ω_i converge with each other at fixed scattering angle $\theta = 120^\circ$.

The effective Compton profiles for Ge atom at photon energy $\omega_i = 662$ KeV with various scattering angle θ are displayed in Fig. 11. We have chosen the scattering angle to be $\theta = 10^\circ, 30^\circ, 60^\circ, 90^\circ, 120^\circ$ and 150° in this figure. Effective Compton profiles $J_{\text{eff}}(p_z, \omega_i, \theta)$ and $J_{\text{sim-eff}}(p_z, \omega_i, \theta)$ defined in Eqs. (32) and (33) with approximate or exact p_z values computed in Eqs. (14) and (13) are plotted the same as in Fig. 10. The nonrelativistic and relativistic atomic Compton profiles have been compared in the figure. In these cases, momentum p_z has maximum and minimum values constrained by energy and momentum conservations, and the maximal kinematically allowed value of p_z increases when scattering angle θ becomes larger. Again in these cases, except that effective Compton profiles $J_{\text{eff}}(p_z, \omega_i, \theta)$ defined in Eq. (32) with exact p_z values fit well with the atomic Compton profiles for all p_z values, other kinds of effec-

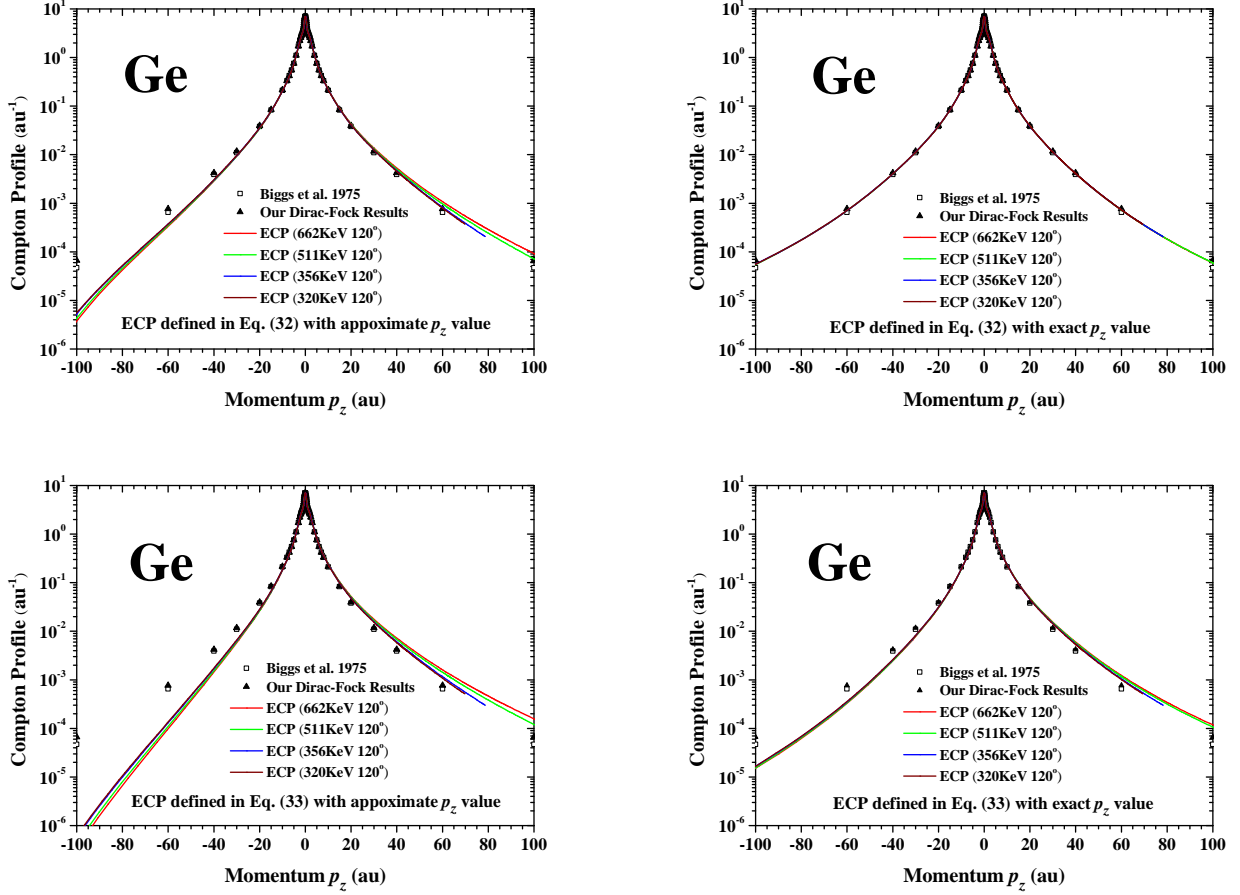


FIG. 10: Effective Compton profiles (ECP) for Ge atom at scattering angle $\theta = 120^\circ$ with various incident photon energy $\omega_i = 662, 511, 356$ and 320 KeV. Upper left panel: effective Compton profile $J_{\text{sim-eff}}(p_z, \omega_i, \theta)$ defined in Eq. (33) with approximate p_z values computed in Eq. (14). Upper right panel: effective Compton profile $J_{\text{sim-eff}}(p_z, \omega_i, \theta)$ defined in Eq. (33) with exact p_z values calculated in Eq. (13). Lower left panel: effective Compton profiles $J_{\text{eff}}(p_z, \omega_i, \theta)$ defined in Eqs. (32) with approximate p_z values. Lower right panel: effective Compton profiles $J_{\text{eff}}(p_z, \omega_i, \theta)$ defined in Eqs. (32) with exact p_z values. Atomic Compton profiles $J(p_z)$ computed using Eq. (20) from nonrelativistic Hatree-Fock (HF) theory and relativistic Dirac-Fock (DF) theory are also plotted as in Fig. 5. Moreover, for various effective Compton profiles, the projective momentum p_z has a maximal cutoff due to the energy and momentum conservations.

tive Compton profiles are not axisymmetric around the $p_z = 0$ axis and have large discrepancies at large $|p_z|$ values. From Fig. 11, it is obvious that effective Compton profiles $J_{\text{sim-eff}}(p_z, \omega_i, \theta)$ defined in Eq. (33) for different scattering angles θ do not converge with each other at a fixed incident photon energy $\omega_i = 662$ KeV. However, we have learned in Fig. 10 that simplified version of effective Compton profiles $J_{\text{sim-eff}}(p_z, \omega_i, \theta)$ for different energies ω_i agree with each other at fixed scattering angle, in-

dicating that effective Compton profiles $J_{\text{sim-eff}}(p_z, \omega_i, \theta)$ are more sensitive to the scattering θ than the incident photon energy ω_i . Moreover, the curves which correspond to smaller scattering angles are more closer to the usual atomic Compton profiles. Furthermore, the same as in Fig. 11, all kinds of effective Compton profiles are consistent with atomic Compton profiles when $|p_z|$ is less than 20 a.u..

-
- [1] M. J. Cooper, *Compton scattering and electron momentum distributions*, Adv. Phys. **20**, 453-491 (1971).
 [2] P. M. Bergstrom Jr. and R. H. Pratt, *An overview of the theories used in Compton Scattering Calculations*, Ra-

- diat. Phys. Chem. **50**, 3-29 (1997).
 [3] M. J. Cooper, *Compton scattering and the study of electron momentum density distributions*, Radiat. Phys. Chem. **50**, 63-76 (1997).

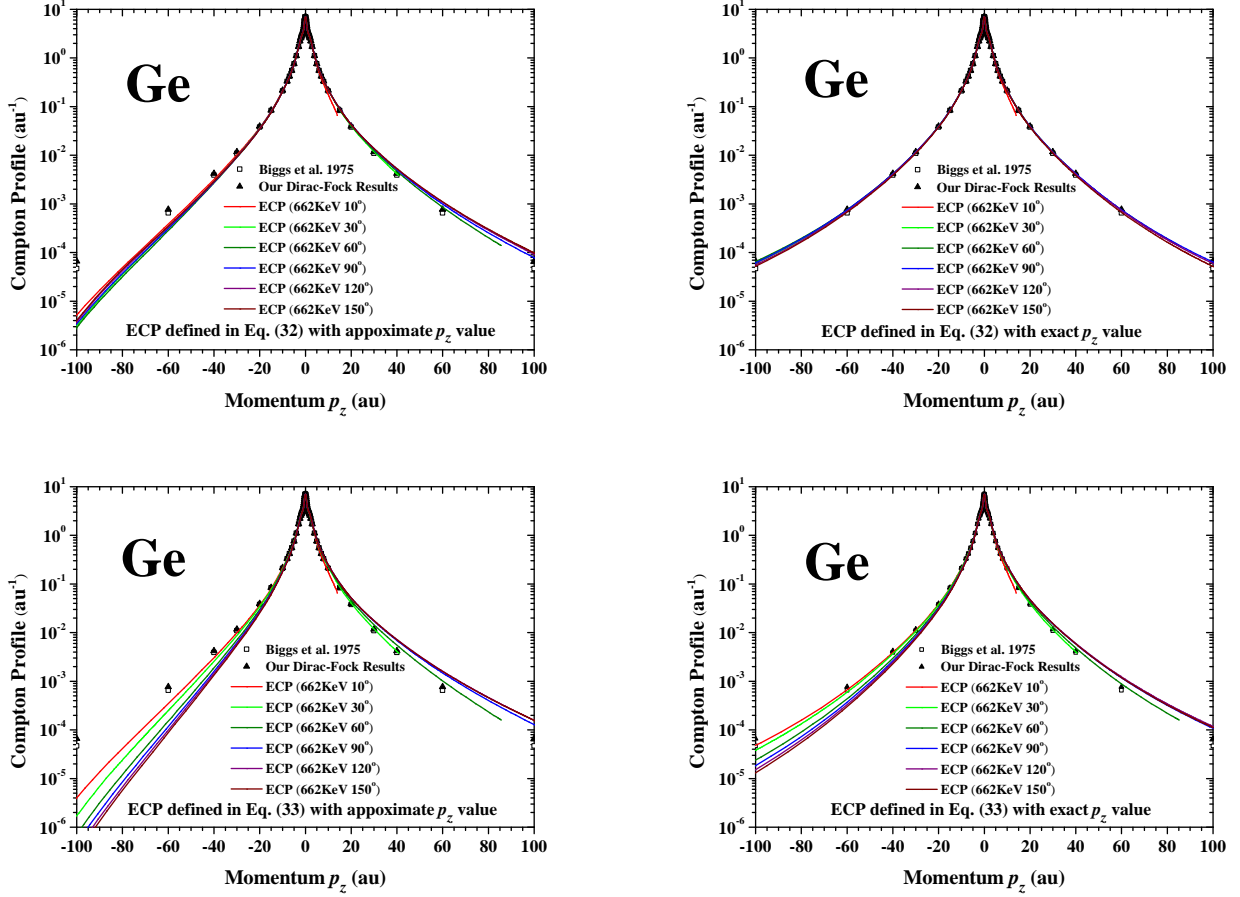


FIG. 11: Effective Compton profiles (ECP) for Ge atom at photon energy $\omega_i = 662$ KeV with various scattering angle $\theta = 10^\circ, 30^\circ, 60^\circ, 90^\circ, 120^\circ$ and 150° . The effective Compton profiles $J_{\text{eff}}(p_z, \omega_i, \theta)$ and $J_{\text{sim-eff}}(p_z, \omega_i, \theta)$ defined in Eqs. (32) and (33) with approximate or exact p_z values computed in Eqs. (14) and (13) are plotted the same as in Fig. 10. Atomic Compton profiles $J(p_z)$ computed using Eq. (20) from nonrelativistic and relativistic theories are also plotted as in Fig. 5.

- [4] J.-M. Gillet, C. Fluteaux, and P. J. Becker, *Analytical reconstruction of momentum density from directional Compton profiles*, Phys. Rev. B **60**, 2345 (1999).
- [5] Y. Kubo, *Electron correlation effects on Compton profiles of copper in the GW approximation*, J. Phys. Chem. Solids **66** 2202-2206 (2005).
- [6] T. Surić, *Compton scattering beyond impulse approximation: Correlation, nonlocal-exchange and dynamic effects*, Radiat. Phys. Chem. **75**, 1646-1650 (2006).
- [7] R. H. Pratt, L. A. LaJohn, V. Florescu, T. Surić, B. K. Chatterjee, S. C. Roy, *Compton scattering revisited*, Radiat. Phys. Chem. **79**, 124-131 (2009).
- [8] Y. J. Wang, H. Lin, B. Barbiellini, P. E. Mijnarends, S. Kaprzyk, R. S. Markiewicz, and A. Bansil, *Proposal to determine the Fermi-surface topology of a doped iron-based superconductor using bulk-sensitive Fourier-transform Compton scattering*, Phys. Rev. B **81**, 092501 (2010).
- [9] A. Rathor, V. Sharma, N. L. Heda, Y. Sharma, and B. L. Ahuja, *Compton profiles and band structure calculations of IV-VI layered compounds GeS and GeSe*, Radiat. Phys. Chem. **77**, 391-400 (2008).
- [10] J. Sahariya and B. L. Ahuja, *Compton profiles and electronic properties of Nd*, Phys. Scr. **84**, 065702 (2011).
- [11] C. Pisani, M. Itou, Y. Sakurai, R. Yamaki, M. Ito, A. Erba, and L. Maschio, *Evidence of instantaneous electron correlation from Compton profiles of crystalline silicon*, Phys. Chem. Chem. Phys. **13**, 933-936 (2011).
- [12] O. Klein, Y. Nishina, *Über die Streuung von Strahlung durch freie Elektronen nach der neuen relativistischen Quantendynamik von Dirac*, Z. Phys. **52** (1929) 853-868.
- [13] J. J. Sakurai, *Advanced Quantum Mechanics* (Addison-Wesley, New-York, 1967).
- [14] P. Eisenberger, W. A. Reed, *Relationship of the relativistic Compton cross section to the electron's velocity distribution*, Phys. Rev. B **9** (1974) 3237.
- [15] R. Ribberfors, *Relationship of the relativistic Compton cross section to the momentum distribution of bound electron states*, Phys. Rev. B **12**, 2067 (1975).
- [16] R. Ribberfors, *Relationship of the relativistic Compton cross section to the momentum distribution of bound electron states-II. Effects of anisotropy and polarization*, Phys. Rev. B **12**, 3136 (1975).
- [17] R. Ribberfors, K.-F. Berggren, *Incoherent-x-ray-*

- scattering functions and cross sections $(d\sigma/d\Omega)_{incoh}$ by means of a pocket calculator, Phys. Rev. A **26**(6), 3325 (1982).
- [18] R. Ribberfors, *X-ray incoherent scattering total cross sections and energy-absorption cross sections by means of simple calculation routines*, Phys. Rev. A **27**, 3061 (1983); Erratum: Phys. Rev. A **28**, 2551 (1983).
- [19] D. Brusa, G. Stutz, J. A. Riveros, J. M. Fernbdez-Varea, F. Salvat, *Fast sampling algorithm for the simulation of photon Compton scattering*, Nucl. Instrum. Meth. A **379**, 167-175 (1996).
- [20] K. Ramanathan, A. Kavner, A. E. Chavarria, P. Privitera, D. Amidei, T.-L. Chou, A. Matalon, R. Thomas, J. Estrada, J. Tiffenberg, and J. Molina, *Measurement of low energy ionization signals from Compton scattering in a charge-coupled device dark matter detector*, Phys. Rev. D **96**, 042002 (2017).
- [21] L. A. LaJohn, *Low-momentum-transfer nonrelativistic limit of the relativistic impulse approximation expression for Compton-scattering doubly differential cross sections and characterization of their relativistic contributions*, Phys. Rev. A **81**, 043404 (2010).
- [22] F. Biggs, L. B. Mendelsohn and J. B. Mann, *Hatree-Fock Compton Profiles for the Elements*, At. Data and Nucl. Data Table **16** 201 (1975).
- [23] W. Rodejohann, *Neutrinoless double-beta decay and neutrino physics*, J. Phys. G: Nucl. Part. Phys. **39** 124008 (2012).
- [24] T. M. Undagoitia and L. Rauch, *Dark matter direct-detection experiments*, J. Phys. G: Nucl. Part. Phys. **43**, 013001 (2015).
- [25] M. Agostini *et al.* (GERDA Collaboration), *Results on Neutrinoless Double- β Decay of ^{76}Ge from Phase I of the GERDA Experiment*, Phys. Rev. Lett. **111**, 122503 (2013).
- [26] M. Agostini *et al.* (GERDA Collaboration), *Improved Limit on Neutrinoless Double- β Decay of ^{76}Ge from GERDA Phase II*, Phys. Rev. Lett. **120**, 132503 (2018).
- [27] S. K. Liu *et al.* (CDEX Collaboration), *Constraints on axion couplings from the CDEX-1 experiment at the China Jinping Underground Laboratory*, Phys. Rev. D **95**, 052006 (2017).
- [28] H. Jiang *et al.* (CDEX Collaboration), *Limits on Light Weakly Interacting Massive Particles from the First $102.8\text{kg} \times \text{day}$ Data of the CDEX-10 Experiment*, Phys. Rev. Lett. **120**, 241301 (2018).
- [29] R. Agnese *et al.* (SuperCDMS Collaboration), *Results from the Super Cryogenic Dark Matter Search Experiment at Soudan*, Phys. Rev. Lett. **120**, 061802 (2018).
- [30] X. Cui *et al.* (PandaX-II Collaboration), *Dark Matter Results from 54-Ton-Day Exposure of PandaX-II Experiment*, Phys. Rev. Lett. **119**, 181302 (2017).
- [31] D. S. Akerib *et al.* (LUX Collaboration), *Results from a Search for Dark Matter in the Complete LUX Exposure*, Phys. Rev. Lett. **118**, 021303 (2017).
- [32] E. Aprile *et al.* (XENON Collaboration), *Dark Matter Search Results from a One Ton-Year Exposure of XENON1T*, Phys. Rev. Lett. **121**, 111302 (2018).
- [33] J. B. Albert *et al.* (EXO-200 Collaboration), *Search for Majorana neutrinos with the first two years of EXO-200 data*, Nature **510**, 229-234 (2014).
- [34] A. Gando *et al.* (KamLAND-Zen Collaboration), *Search for Majorana Neutrinos Near the Inverted Mass Hierarchy Region with KamLAND-Zen*, Phys. Rev. Lett. **117**, 082503 (2016), Erratum: Phys. Rev. Lett. **117**, 109903 (2016).
- [35] P. Eisenberger and P. M. Platzman, *Compton Scattering of X Rays from Bound Electrons*, Phys. Rev. A **2**, 415 (1970).
- [36] P. M. Bergstrom Jr., T. Surić, K. Pisk, and R. H. Pratt, *Compton scattering of photons from bound electrons: Full relativistic independent-particle-approximation calculations*, Phys. Rev. A **48**, 1134 (1993).
- [37] M. Jung, R. W. Dunford, D. S. Gemmell, E. P. Kanter, B. Krässig, T. W. LeBrun, S. H. Southworth, L. Young, J. P. J. Carney, L. LaJohn, R. H. Pratt, and P. M. Bergstrom Jr., *Manifestations of Nonlocal Exchange, Correlation, and Dynamic Effects in X-Ray Scattering*, Phys. Rev. Lett. **81**, 1596 (1998).
- [38] I. G. Kaplan, B. Barbiellini, and A. Bansil, *Compton scattering beyond the impulse approximation*, Phys. Rev. B **68**, 235104 (2003).
- [39] E. G. Drukarev, A. I. Mikhailov, and I. A. Mikhailov, *Low-energy K-shell Compton scattering*, Phys. Rev. A **82**, 023404 (2010).
- [40] T. Surić, P. M. Bergstrom Jr., K. Pisk, and R. H. Pratt, *Compton scattering of photons by inner-shell electrons*, Phys. Rev. Lett. **67**, 189 (1991).